Positron Emission Tomography Partial Volume Correction: Estimation and Algorithms

John A. D. Aston[†], Vincent J. Cunningham[§], Marie-Claude Asselin[§], Alexander Hammers[§], Alan C. Evans[†], and Roger N. Gunn[†]

[†]McConnell Brain Imaging Center, Montreal Neurological Institute, McGill University, Montreal, Canada

[§]Imaging Research Solutions Ltd., Cyclotron Building, Hammersmith Hospital, London, U.K.

Abstract

Partial Volume Effects in PET lead to quantitative under and over estimations of the regional concentrations of radioactivity in reconstructed images and corresponding errors in derived functional or parametric images. The limited resolution of PET leads to "Tissue Fraction" effects, reflecting underlying tissue heterogeneity, and "Spillover" effects between regions. Addressing the former problem in general requires supplementary data, for example coregistered high-resolution MR images, whereas the latter effect can be corrected for with PET data alone if the point spread function of the tomograph has been characterised. Analysis of otherwise homogeneous region of interest data ideally requires a combination of tissue classification and correction for the point spread function. The formulation of appropriate algorithms for partial volume correction (PVC) is dependent on both the distribution of the signal and the distribution of the underlying noise. A mathematical framework has therefore been developed to accommodate both of these factors and to facilitate the development of new PVC algorithms based on the description of the problem. Several methodologies and algorithms have been proposed and implemented in the literature in order to address these problems. These methods do not, however, explicitly consider the noise model whilst differing in their underlying assumptions. The general theory for estimation of regional concentrations, associated error estimation and inhomogeneity tests are presented in a weighted least squares framework. The analysis has been validated using both simulated and real PET data sets. The relationships between the current algorithms and those published previously are formulated and compared. The incorporation of tensors into the formulation of the problem has led to the construction of computationally rapid algorithms taking into account both tissue fraction and spillover effects. The suitability of their application to dynamic and static images is discussed.

Keywords: *PET, Partial Volume Correction, Point Spread Function, Tissue Classification, Noise Models, 3-D Algorithms*

1 Introduction

This paper is concerned with theory and methodology for the recovery of partial volume effects in positron emission tomography (PET). The partial volume correction (PVC) problem in PET concerns two properties, both arising from the limited resolution of the tomograph, which result in incorrect estimation of the true local tissue concentration of radioactivity;

"Tissue Fraction Effect" referring to underlying sub-resolution heterogeneity, for example grey and white matter in brain tissue. In general, correction for this effect requires additional prior knowledge, for example from an adjunct MRI scan with intrinsically higher resolution enabling determination of the appropriate tissue fractions.

"Point Spread Effect" or spillover between regions, again reflecting the limited resolution of the tomograph (Hoffman et al., 1979; Mazziotta et al., 1981; Leahy and Qi, 2000). Typically the PSF is well approximated by a 3-dimensional Gaussian distribution with FWHM of the order of a few millimeters. This effect can in principle be corrected from the PET data alone, assuming that the point spread function of the scanner has been characterised.

It is convenient to distinguish these effects, firstly because the resolution of the tissue fraction effect will require data in addition to the PET measurements, and secondly because it will be seen to have statistical consequences in our analysis. However, they are both a result of the limited resolution of the scanner, and as such are considered by some to be the same effect.

Recovery of the true concentrations of radioactivity in otherwise homogeneous regions thus requires a combination of tissue classification techniques with corrections for spillover between adjacent regions. The consequences of these effects on the signal have been investigated previously (Karp et al., 1991; Rousset et al., 1993; Iida et al., 2000), and a variety of correction methods, of differing complexities, have been proposed and applied to attempt accurate recovery of the signal in situations where regions are either defined by anatomy, by tissue type, or both (Meltzer et al., 1990; Muller-Gartner et al., 1992; Labbé et al., 1996; Labbé et al., 1998; Rousset et al., 1998). These methods often require structural imaging although methods have been developed (Iida et al., 2000) that do not. In PET the correction is usually applied on a regional level to the reconstructed images and includes regional homogeneity assumptions, which makes the problem more tractable than at the voxel level. Such corrections can have significant impact on the quantitative analysis of PET studies (Labbé et al., 1996; Meltzer et al., 2000; Law et al., 2000), particularly when it is necessary to take into account the effects of pathological or structural changes. Upwards of 300% increases in estimates of cerebral metabolism of $[^{18}F]$DOPA after PVC have been reported (Rousset et al., 2000). PVC has also being explored as a tool for recovery of the input function from PET images (Asselin et al., 2001). Indeed, in any study where true quantitative parameter estimates are required, the implementation of PVC is essential.

There are however, differences in the published methods, particularly as regards the implicit assumptions that are made about the underlying noise models. It will be seen in the present work that the assumed noise model has a direct impact on the appropriate algorithm to use for PVC.

This paper introduces a theoretical framework for the general PVC problem and presents new and improved algorithms for the application of PVC techniques to static and dynamic PET

images. Both the tissue fraction effect and the point spread effect are accommodated within this analysis. Previous methods are discussed within this theoretical framework. In addition, methods for error estimation are presented and regional inhomogeneity testing is investigated. The general theory for estimation of regional radioactivity concentrations, associated error estimation and inhomogeneity tests are presented in a weighted least squares framework. Regional inhomogeneity testing allows for the statistical assessment of the methods assumption that all regions are homogeneous in concentration. Finally, an efficient tensor algorithm allowing for the application of these methods in 3-D is also presented. This new analysis is validated using both simulated and experimental PET data.

2   Theory

Partial volume correction in PET will be considered with reference to both the distribution of the signal and the underlying noise model. The formulation of algorithms for the solution of the PVC problem is dependent on both of these factors. Noise needs to be considered in terms of both its distribution and its structure. Several noise distributions have been proposed in the past for simulation of the problem; Poisson, Gaussian and Poisson + Gaussian (Slifstein et al., 2001). Here, not only are the noise distributions but also the correlation structure of the noise investigated and algorithms formulated for these differing structures.

2.1   Noise Models

The measurement of PET data is an inherently noisy process. Radioactive decay is itself a random process with a Poisson distribution, and other distributions of noise enter the system at many stages of data collection and reconstruction. In the present paper, two structures are considered. First, if the noise is inherent in the signal, before any reconstruction has taken place, then it is considered that this noise will be subject to blurring due to the PSF and will result in spatially correlated noise in the reconstructed image. Second, noise occurring across the reconstructed image on a random basis will be modelled with an additive term with no spatial correlation.

- **Uncorrelated Noise Models.** This noise model assumes that there is additive Gaussian noise across the reconstructed image and corresponds to high spatial frequency noise. Previous methods (Labbé et al., 1996; Labbé et al., 1998; Rousset et al., 1998) are implicitly based on this model although slightly different weights are applied to obtain the solution. (see 2.3).

- **Correlated Noise Models.** There will be a component in the noise that is correlated by the point spread function. This could arise from the signal itself, or other noisy processes that become blurred by the PSF. We will also include an uncorrelated component in the model to allow for any high spatial frequency noise, which would cause an ill-conditioned solution in not appropriately accounted for. The limit of this model is a purely PSF correlated noise model, but as has been previously seen (Leahy and Qi, 2000), this does not adequately describe the true noise in the data.

For our algorithms, whether the noise is homogeneous across the image, or whether heterogeneous is immaterial. There is evidence that the variance is homogeneous across image (Pajevic et al., 1998). Previous work has detailed methods for the approximation of ROI and pixelwise variance (Carson et al., 1993). In fact this specifies the correlation function between pixels and as such can be used as the correlation function in the algorithms themselves. A specification needs to be made prior to the analysis, but the analysis itself will proceed in the same way. For the data presented later, the noise models will assume either homogeneous or hetergeneous variances across the image but include a homogeneous uncorrelated variance component.

2.2   The 1-D Problem

The problem is first formulated in 1 dimension for simplicity. It will be seen that given a separable point spread function the problem generalizes simply to 3 dimensions. The correlation function has been assumed, for simplicity, to be accurately characterised by the PSF, but any separable correlation function can be modelled in this framework. Let P be an $n \times n$ matrix, where n is the number of pixels, whose operation on a vector corresponds to the blurring introduced by the PSF. For a symmetric spatially invariant PSF this is a symmetric Toeplitz matrix, although other more general PSF distributions can be accommodated. Let R be an $n \times r$ matrix defining r anatomical regions ($R \in [0,1]$). Let T be an $n \times t$ matrix denoting the t different tissue classifications, ($T \in [0,1]$). Let b be an $n \times 1$ vector containing the measured tracer concentration. Consequently x is an $rt \times 1$ vector denoting the true radioactivity concentrations in the different classified regions. As constructed, P accounts for the "Point Spread Effect", $R \odot T$ account for the "Tissue Fraction Effect", where $\odot$ is the Khatri-Rao row product (see Appendix B.2). The tracer concentration is assumed to be homogeneous within each classified region. A simple example is presented in Figure 1a which illustrates how the measured tracer concentrations may be an under- or over-estimation of the true concentration.

The partial volume problem can then be constructed as a matrix equation, (Figure 1b),

$$P(R \odot T)x = b, \tag{1}$$

and the introduction of noise components gives,

$$P((R \odot T)x + \eta_c) = b + \eta_u, \tag{2}$$

where η_c and η_u are correlated and uncorrelated noise vectors respectively (see section 2.1). This equation can be rearranged in terms of the recovered signal and noise components[1],

$$(R \odot T)x = P^{-1}b + (P^{-1}\eta_u + \eta_c), \tag{3}$$

and is a linear equation of the form $Ax = b + \epsilon$.

The weighted linear least squares solution, x, is determined by minimising the objective function,

$$\min_x \quad (W^{\frac{1}{2}}((R \odot T)x - P^{-1}b))^T(W^{\frac{1}{2}}((R \odot T)x - P^{-1}b)), \tag{4}$$

---

[1]η_x represents the noise process and hence the sign is unimportant here
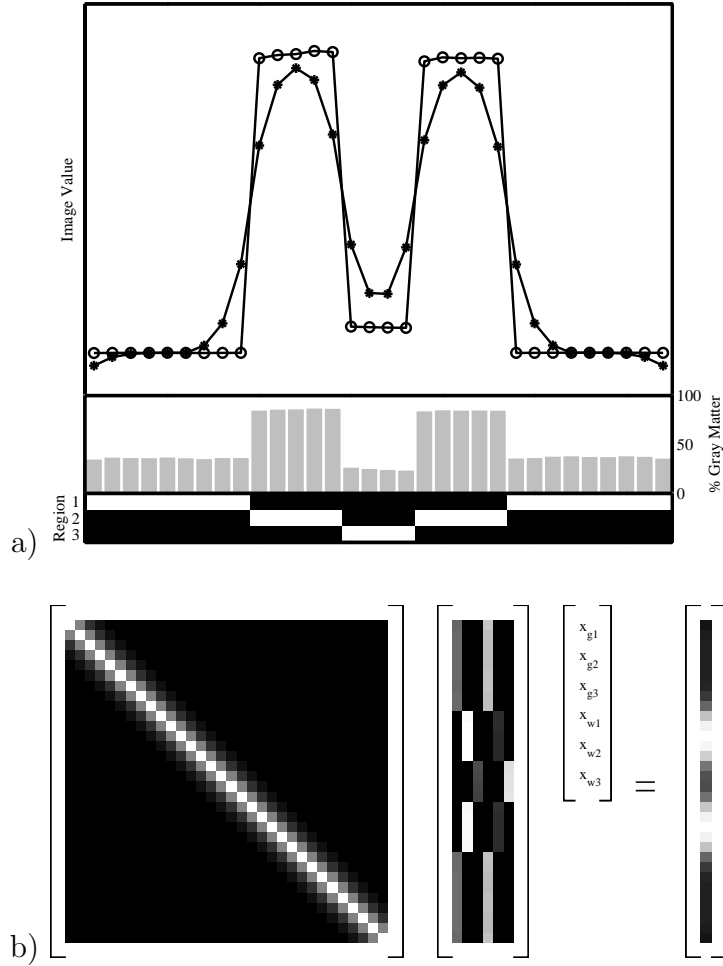
FIGURE 1: 1D PVC Example: a) (top) Tissue Radioactivity with (*) and without (o) application of PSF, (middle) Tissue Classification (Grey and White only), (bottom) Region Definitions b) Matrix construction of the recovery problem, where x_{gi} and x_{wi} are the recovered grey and white matter values respectively for region i.

where the weighting matrix W is the inverse of the covariance matrix and the solution is given by,

$$\hat{x} = ((R \odot T)^T W (R \odot T))^{-1} (R \odot T)^T W P^{-1} b. \tag{5}$$

It follows that the variance on the estimates is given by,

$$var(\hat{x}) = \frac{((R \odot T)^T W (R \odot T))^{-1} ((R \odot T)x - P^{-1}b)^T W ((R \odot T)x - P^{-1}b)}{n - rt}, \tag{6}$$

and the sum of squares accounted for by each ROI is given by,

$$SSQ_{ROI} = ((R \odot T)x - P^{-1}b)^T W^{\frac{1}{2}} \Lambda(R_{ROI}) W^{\frac{1}{2}} ((R \odot T)x - P^{-1}b) \tag{7}$$

where $\Lambda()$ is the diagonal matrix operator, and ROI is the index of the region to be tested.

The above equations are all theoretically consistent, and in practice can be used to evaluate partial volume effects. It is interesting to note however, that the equations only hold true when $R \odot T$ is a full rank matrix. This might occur (theoretically), for example, if the grey and

white composition was constant in a given region. However as the grey and white classification is probabilistic, and the regions sizes are greater than a few voxels, this is not a problem in practice.

The recovered values for the regionally classified tissues may be estimated once an appropriate noise model has been selected (Eqn 5). The noise model determines the form of the weighting matrix W. It should be noted here that it is of increasing importance that the noise model is estimated correctly to ensure accurate estimates of the parameters above. Hence the accuracy of the weighting is of limited importance for the estimate of tracer concentration (Eqn 5 & Figure 2). This results in good estimates from both Labbé and Rousset's methods. However, it is more important for estimation of the error on this value (Eqn 6 & Figure 2) and of vital importance for hypothesis testing of homogeneity derived from the residual sum of squares (Eqn 7).

2.2.1 Uncorrelated noise: $[\eta_u \sim N(0, \sigma_u^2 I) \text{ and } \eta_c = 0]$

If the noise on the measured image is characterised purely by independent identically distributed Gaussian processes with zero mean and standard deviation σ_u then the weighting matrix is given by,

$$W = P^T P, \tag{8}$$

and the weighted least squares solution is,

$$\hat{x} = ((R \odot T)^T P^T P (R \odot T))^{-1} (R \odot T)^T P^T b. \tag{9}$$

2.2.2 Pure correlated noise: $[\eta_c \sim N(0, D) \text{ and } \eta_u = 0]$

If the noise post reconstruction has no uncorrelated component then

$$W = D^{-1} \tag{10}$$

where D is a diagonal matrix representing variances at each pixel (can be homogeneous or inhomogeneous).

The weighted least squares solution is,

$$\hat{x} = ((R \odot T)^T D^{-1} (R \odot T))^{-1} (R \odot T)^T D^{-1} P^{-1} b. \tag{11}$$

2.2.3 Correlated noise: $[\eta_c \sim N(0, D) \text{ and } \eta_u \sim N(0, \sigma_u^2 I)]$

If the noise on the image is characterised by both independent identically distributed Gaussian processes then the weighting matrix is given by,

$$W = (D + \sigma_u^2 P^{-1} (P^{-1})^T)^{-1}, \tag{12}$$

and the weighted least squares solution is,

$$\hat{x} = ((R \odot T)^T (D + \sigma_u^2 P^{-1}(P^{-1})^T)^{-1}(R \odot T))^{-1} \tag{13}$$
$$(R \odot T)^T (D + \sigma_u^2 P^{-1}(P^{-1})^T)^{-1} P^{-1} b.$$

If any part of the noise structure is signal dependent, then the recovered signal needs to be known. These equations assume that the value for this signal is known. As this will not be the case in heterogeneous signal-dependent noise such as poisson noise, the solution requires an iterative solution using updates of the estimates, known as Fisher Scoring (McCullagh and Nelder, 1989). This is easily incorporated into the algorithms described.

2.3 The Methods of Labbé and Rousset

The methods of both Labbé (Labbé et al., 1996) and Rousset (Rousset et al., 1998) and their solutions to the general partial volume correction problem,

$$P(R \odot T)x = b, \tag{14}$$

can be characterised by their implicit weighting matrices, W, in the weighted least squares framework (Eqn 4 & 5).

2.3.1 Rousset's Method

The solution given by Rousset is,

$$x = ((R \odot T)^T P(R \odot T))^{-1}(R \odot T)^T b, \tag{15}$$

which is equivalent to a weighted least squares solution in which,

$$W = P. \tag{16}$$

2.3.2 Labbé's Method

The solution given by Labbé is,

$$x = ((R \odot T)^T P^T P(R \odot T))^{-1}(R \odot T)^T P^T b \tag{17}$$

which is equivalent to a weighted least squares solution in which,

$$W = P^T P, \tag{18}$$

and can be interpreted as the ordinary least squares solution to the problem.
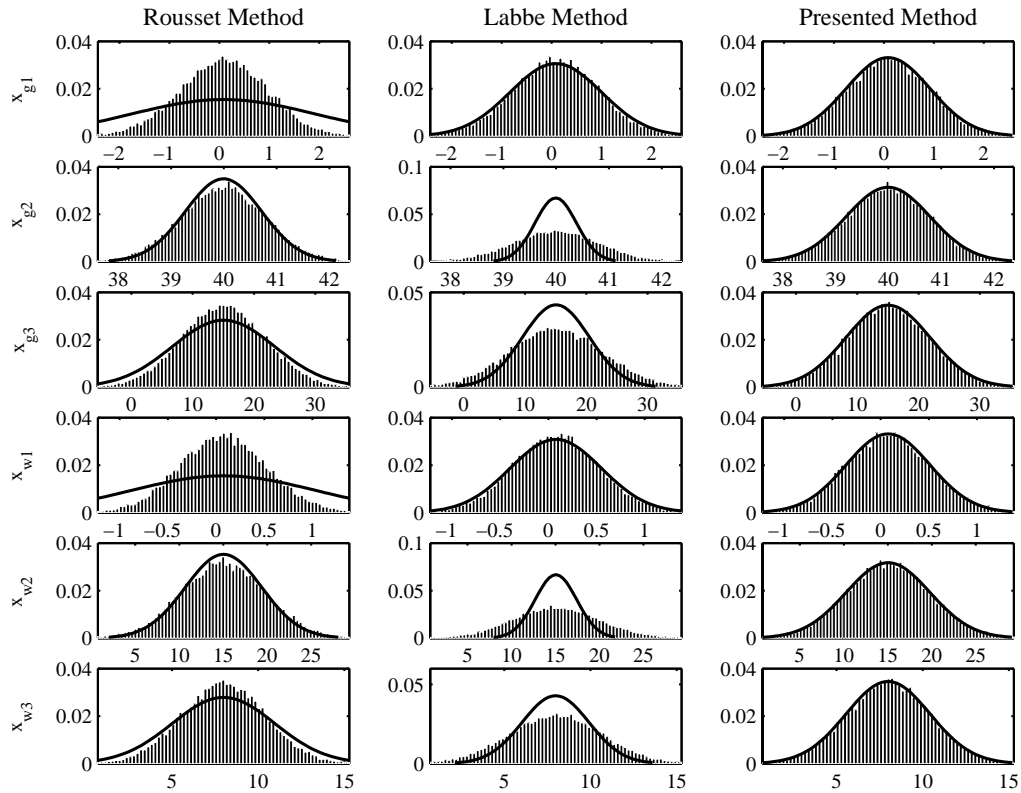
FIGURE 2: 1D PVC Example: Noise Distribution. Histogram: Estimated values, Solid Line: Expected Theoretical Parameter Distribution. X-axis: estimated parameter values, Y-axis: probability. This data is simulated using a heterogeneous correlated and homogeneous un-correlated noise model. The presented method uses this noise structure, whilst the methods of Labbe and Rousset have implicit assumptions about the noise. This figure is intended as a graphical representation of the performance of the differing methods in differing noise situations.

2.4   1-D Simulations

The one dimensional simulations presented here are primarily to demonstrate the problems that can occur if the wrong noise model is assumed when fitting the data, in terms of the estimation of the mean and variance. Although the noise model here is a proportional model, where the noise is proportional to the signal, the underlying problems will also be evident with other noise models.

Simulations were carried out using the example signal representation above. This was done in order that there would be regions where the signal was both over and under estimated. Noise was added which had both a homogeneous uncorrelated component, and a heterogeneous (proportional to the signal) correlated component. The data sets were then simulated with 25000 repetitions to build up accurate distributions from each of the estimators.

As can be seen in the figure (Figure 2) if the noise model is incorrect, the estimates of the variance of the signal estimate are not correct. The histograms represent the true distribution of the estimate of the value whilst the solid lines represent the estimated distribution. As can be seen, the variance of true distributions are either under or over estimated by the Rousset

and Labbé algorithms, and different regions have different over / under estimation. This is due to the implicit assumptions of the model. The Labbé algorithm assumes uncorrelated noise, and as such the background as the largest region dominates this noise resulting in a good estimate of the background noise, but underestimation in regions of higher noise. The Rousset algorithm has the assumption that the noise is inversely correlated from smoothing, and as such over-estimates the variance in regions with low noise and under-estimates the variance in regions with higher noise. However the estimates of the signal itself is unbiased for the differing estimators.

2.5   Generalization to 3-Dimensions

The theory above has been presented in terms of the 1-Dimensional case. A consideration of the assumptions which allows the theory to be generalized to 3-Dimensions follows. The only assumption to allow the full generalization of the above theory is that each dimension is separable from all the other dimensions. This means that the PSF operator may be applied independently in the x,y and z dimensions. This assumption is weaker than the assumptions that are made in some previous methods where stationarity is also assumed to facilitate computation (Labbé et al., 1996). However this assumption was partially removed in later work (Labbé et al., 1998).

It is important to consider other computational aspects which allow for the higher dimension generalization. It is straightforward to see how the computation is handled in the 1-D case with simple matrix and vector operations. The 3-D equivalent is simplified by considering tensor[2] operations with restrictive separable properties. Such a construction leads to a computationally efficient algorithm for the implementation of 3-D partial volume correction (see Appendix A.1).

3   Methods

The above theory and algorithms were applied to several data sets for the purpose of validation. Both simulated and measured data were used, primarily with the same specifications, except that in the simulated data sets, the noise characteristics were known perfectly, whilst in the measured data sets, the noise characteristics were assumed to be fully characterised.

3.1   Simulated Data Sets

Two simulated data sets were considered. The first consisted of a set of four syringes of differing diameters and considers merely the "Point Spread Effect" and required only the definition of R. The second is a flumazenil brain phantom which considered both the "Point Spread" and "Tissue Fraction" effects and required the definition of both R and T. The simulated data sets were primarily specified using the corresponding measured data sets. The noise variances were determined approximately from the measured data, and then the linear model to be solved

---

[2]Tensors are merely generalizations of vectors (1D) and matrices (2D) in higher dimensions

was constructed to produce simulated realizations with the exact noise characteristics for the weighting matrix.

3.1.1 Syringe Phantom

The Syringe Phantom data were simulated realisations of the measured data obtained from the ECAT ART scanner. The reported PSF characteristics (Bailey et al., 1997) for the ART scanner were used to specify the PSF as a Gaussian kernel, both in the construction of the data set and the subsequent fitting procedures of the algorithms. This allowed for perfect specification of the PSF. The syringe ROIs were generated as cylinders corresponding to the size and location of their counterparts in the physical phantom (Figure 3). The syringes were simulated to contain 75 kBq/ml of activity at the start of the first acquisition. Noise was added to the images to approximate the measured data for different epochs in time, each epoch being separated by a tracer half life (in this case 20 mins for Carbon-11). This generated data with a progressively decreasing signal to noise ratio. Homogeneous correlated noise was introduced before applying the PSF and subsequently uncorrelated noise was added. The variance of the noise was based on the background noise in the actual measured images at the times of acquisition. Analysis was performed on non-decay corrected data, whilst the results were decay corrected for ease of comparison. The analysis was carried out using the presented algorithms, as well as Labbé and Rousset's algorithms, to recover the signal and the error estimates. The simulations were also used to assess the possibility of homogeneity testing in well defined noise models. This was assessed using both the entire dataset and a single syringe ROI and it was determined whether the expected distribution was obtained using the Krylov approximation model (see Appendix A.3).
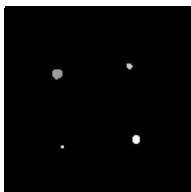

FIGURE 3: Definition of the 5 regions (including background) for the syringe data set represented by different grey levels (corresponding to R).

3.1.2 Flumazenil Phantom via MRI segmentation

The flumazenil simulation was generated using the measured flumazenil data set analysed below. The data was simulated using the region definitions (R) combined with the tissue classifications (T) (Figure 4) . The simulated V_D values were taken from the measured results. It was then smoothed with the assumed PSF. The noise added was also taken from the noise estimate of the real data. The presented analysis was again used, in a similar way to the syringe data. The estimated noise characteristics of the real model were used to describe the noise in the simulations. The Krylov inhomogeneity testing requires a known variance, and in this case where the variance is estimated, its use is not applicable.
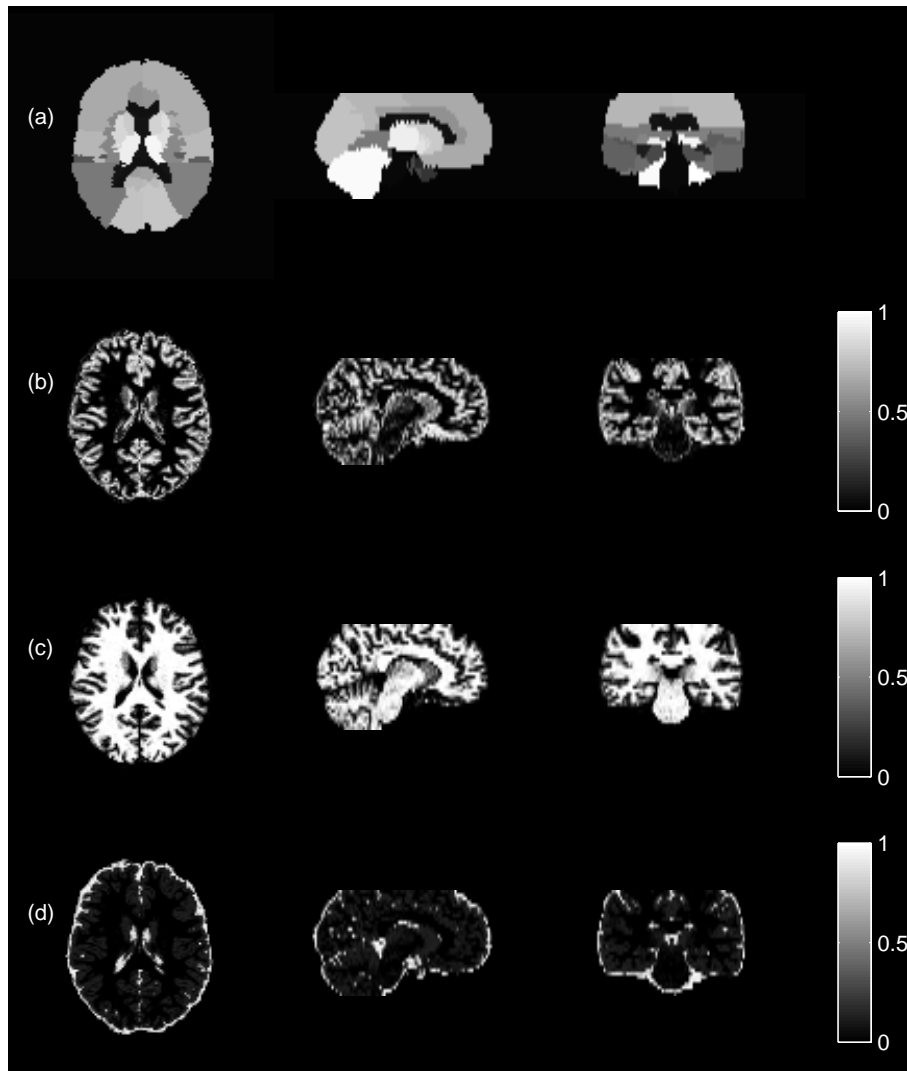
FIGURE 4: Flumazenil Data Set : (a) Definition of the 43 regions for the flumazenil data set represented by different grey levels (corresponding to R). (b) grey (c) white and (d) CSF tissue classification probabilities (corresponding to T).

3.2 Measured Data Sets

3.2.1 Syringe Phantom

Four syringes of inner diameters 14.8+/-0.1mm, 11.9+/-0.1mm, 8.6+/-0.1mm and 4.7+/-0.1mm were filled with a C-11 solution (75 kBq/ml at the start of the first acquisition) and inserted into a 20-cm diameter 30-cm long cylinder filled with water. The phantom was scanned in an ECAT ART tomograph (CTI/Siemens, Knoxville, TN, USA) for 10s and 120s, four times, one half life (20 min) apart each time (Figure 5). The images were reconstructed using the reprojection algorithm (Kinahan and Rogers, 1989) with the ramp and Colscher filters set at Nyquist cut-off frequency. A calculated attenuation correction and a model-based scatter correction (Watson et al., 1996) were applied to the data during reconstruction. The reconstructed images consisted of 47 planes (of which only the centre seven were used in the analysis) having a transaxial spatial resolution of 6.7 mm (at 5 cm from the centre of the FOV where the syringes

were located) and an axial spatial resolution of 6.8 mm (FWHM) (Bailey et al., 1997). The presented analysis was again used to calculate the recovery and errors and compared with the methods of Labbé and of Rousset. To assess whether the specified noise model was accurate the Krylov algorithms were applied to the measured data. This was again done on the both the entire data set, and the single syringe as in the simulations above.
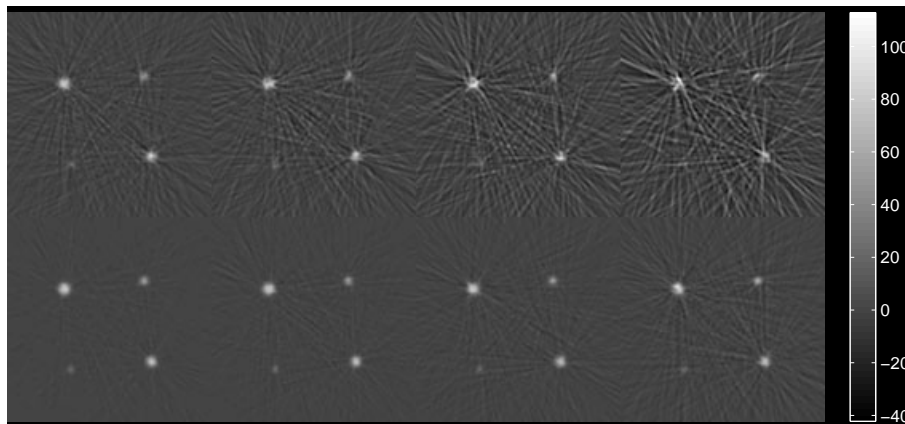

FIGURE 5: Measured Syringe Data: (top) 10s acquisitions (one half life apart), (bottom) 120s acquisitions (one half life apart).

3.2.2   Measured Flumazenil

AAn [^{11}C]Flumazenil data set was obtained from an ongoing clinical study and acquired according to a protocol described previously (Koepp et al., 1996; Richardson et al., 1996). Briefly, the scan was performed in 3D mode on a 953 B Siemens/CTI PET camera with a reconstructed image resolution of approximately 4.8x4.8x5.2 mm at FWHM (Bailey, 1992) for 31 simultaneously acquired planes with reconstructed voxel sizes of 2.09x2.09x3.42 mm. A convolution subtraction method was used to correct for scatter (Bailey and Meikle, 1994) and axial scaling with the inverse of the scanner's axial profile was applied to obtain uniform efficiency throughout the field of view (Grootoonk, 1995). Voxel-by voxel parametric images of [^{11}C]flumazenil volume-of-distribution (V_D) were then produced from the brain uptake and arterial metabolite-corrected plasma input functions using a single compartmental tracer kinetic model and estimates of the variance of the parameters calculated (Aston et al., 2000) and is shown in Figure 6. A region template containing 43 regions was used which was derived from the MRI of a single brain (Holmes et al., 1998) which has been widely used as a reference brain. To subdivide the flumazenil data set, the region template was spatially warped to fit the individual's MRI data set. This was performed using linear and nonlinear transformations (Ashburner and Friston, 1999) with parameters derived from the MRI data set associated with the template (Hammers et al.,). The individuals own MRI was also segmented (Lemieux et al., 1999) into grey matter, white matter and CSF. The transformed region template and the MRI data sets were then coregistered with the PET data set (Ashburner and Friston, 1997). PVC to recover the corrected V_D values was applied using weights derived from the variance map calculated as part of the analysis. Again, the Krylov method was not appropriate for this dataset, due to its unknown variance.
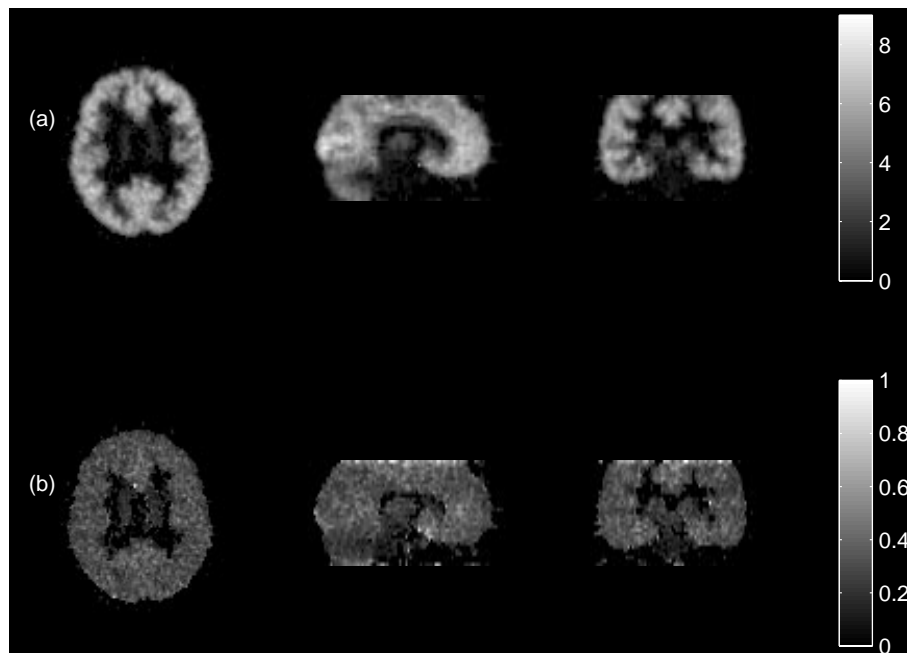
FIGURE 6: Flumazenil: (a) Volume of Distribution; (b) Volume of Distribution Error; prior to correction.

All data analysis was performed in Matlab (The Mathworks Inc.) running on a 650 MHz Pentium PC.

4 Results

In all the studies it was found that the purely correlated noise algorithms were unstable in the presence of uncorrelated noise in the data. This is due to the ill-conditioned nature of the inverse of the correlation matrix. As all the data were assumed to have a true noise structure that included a component of uncorrelated noise, the results of purely correlated algorithms have been omitted due to their instability. This result was not unexpected, and in practice purely correlated noise algorithms are seldom if ever used to analyze data.

4.1 Simulated Data Sets

4.1.1 Syringe Phantom

The syringe simulations showed that good recovery of the true signal was achieved with all algorithms (Table 1), at different times, with earlier frames, where there are more counts, providing yielding closer to truth estimates than later frames (all frames are decay corrected back to the start). However, the estimates of the standard deviation in the Labbé and Rousset algorithms were too low, which would lead to the rejection of null hypotheses with the true mean in some cases. This did not occur with the presented algorithm.

| Method | Time | | 14.8mm | | | 11.9mm | | | 8.6mm | | | 4.7mm | | | Bgd | | |
	Start	Dur	NC	$\hat{x}$	$sd(\hat{x})$	NC	$\hat{x}$	$sd(\hat{x})$	NC	$\hat{x}$	$sd(\hat{x})$	NC	$\hat{x}$	$sd(\hat{x})$	NC	$\hat{x}$	$sd(\hat{x})$
Rousset	0	10	52.4	74.8	0.17	48.6	76.4	0.22	36.8	73.4	0.35	17.9	68.6	0.87	0.12	-0.023	0.007
Labbe	0	10	52.4	74.7	0.27	48.6	76.5	0.37	36.8	73.5	0.62	17.9	71.1	1.73	0.12	-0.023	0.011
Presented	0	10	52.4	74.8	0.77	48.6	76.3	0.98	36.8	73.1	1.47	17.9	69.7	3.48	0.12	-0.023	0.035
Rousset	10	120	52.7	75.1	0.09	48.0	75.4	0.12	37.9	75.5	0.20	19.5	74.5	0.49	0.15	0.010	0.004
Labbe	10	120	52.7	75.2	0.08	48.0	75.4	0.11	37.9	75.6	0.19	19.5	73.5	0.51	0.15	0.010	0.003
Presented	10	120	52.7	75.1	0.23	48.0	75.4	0.29	37.9	75.3	0.44	19.5	74.4	1.04	0.15	0.011	0.010
Rousset	1200	10	51.3	73.2	0.23	46.8	73.6	0.29	39.4	78.7	0.47	22.4	85.9	1.17	0.09	-0.052	0.009
Labbe	1200	10	51.3	73.1	0.39	46.8	73.5	0.53	39.4	79.9	0.89	22.4	83.9	2.47	0.09	-0.057	0.015
Presented	1200	10	51.3	73.2	1.11	46.8	73.6	1.40	39.4	78.3	2.10	22.4	86.1	4.98	0.09	-0.046	0.050
Rousset	1210	120	52.6	75.0	0.10	48.1	75.5	0.13	37.7	75.2	0.21	19.5	74.7	0.53	0.16	0.020	0.004
Labbe	1210	120	52.6	74.9	0.11	48.1	75.5	0.15	37.7	75.2	0.25	19.5	73.9	0.71	0.16	0.021	0.004
Presented	1210	120	52.6	75.1	0.32	48.1	75.5	0.40	37.7	75.2	0.60	19.5	74.7	1.42	0.16	0.020	0.014
Rousset	2400	10	53.0	75.5	0.31	49.1	77.1	0.40	40.5	80.7	0.64	20.3	77.6	1.60	0.23	0.085	0.013
Labbe	2400	10	53.0	75.5	0.55	49.1	77.2	0.74	40.5	80.6	1.25	20.3	75.0	3.47	0.23	0.084	0.021
Presented	2400	10	53.0	75.1	1.55	49.1	77.4	1.96	40.5	80.8	2.94	20.3	79.6	6.96	0.23	0.087	0.071
Rousset	2410	120	52.2	74.4	0.12	47.0	73.9	0.15	38.0	75.7	0.24	19.5	74.8	0.61	0.09	-0.052	0.005
Labbe	2410	120	52.2	74.3	0.16	47.0	73.8	0.21	38.0	75.5	0.36	19.5	76.2	0.99	0.09	-0.053	0.006
Presented	2410	120	52.2	74.5	0.44	47.0	74.1	0.56	38.0	75.8	0.84	19.5	75.3	2.00	0.09	-0.052	0.020
Rousset	3600	10	51.9	74.0	0.42	47.9	75.2	0.55	36.5	72.8	0.88	17.0	65.2	2.19	0.14	0.004	0.018
Labbe	3600	10	51.9	74.2	0.77	47.9	74.0	1.04	36.5	70.9	1.76	17.0	63.7	4.88	0.14	0.004	0.030
Presented	3600	10	51.9	74.0	2.18	47.9	75.8	2.76	36.5	73.7	4.14	17.0	65.4	9.82	0.14	0.007	0.099
Rousset	3610	120	52.7	75.2	0.14	47.4	74.5	0.19	38.0	75.8	0.30	18.9	72.4	0.75	0.16	0.020	0.006
Labbe	3610	120	52.7	75.4	0.22	47.4	74.5	0.29	38.0	75.5	0.50	18.9	73.8	1.38	0.16	0.020	0.008
Presented	3610	120	52.7	75.0	0.62	47.4	74.4	0.78	38.0	75.8	1.17	18.9	71.9	2.78	0.16	0.020	0.028

TABLE 1: Results from partial volume correction of simulated syringe data (Syringe diameters 14.8, 11.9, 8.6 and 4.7mm) from Rousset, Labbé and Presented method: value with no correction (NC) value after correction ($\hat{x}$) and estimated standard deviation of value ($sd(\hat{x})$). True activity value in all the syringes was 75 kBq/ml (at $t = 0$, all values are decay corrected to $t = 0$). Units are kBq/ml.
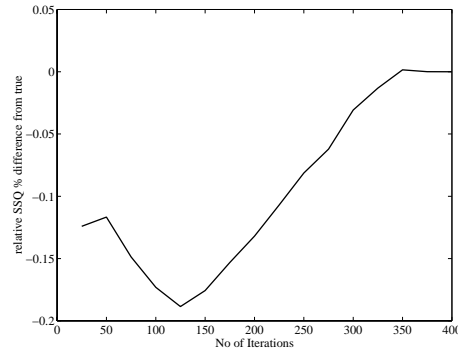
FIGURE 7: Typical Krylov interations for simulated syringe.

The presented algorithm took approximately 10 mins per frame to run. This is dependent on the noise model, as can be seen in equation 26 in the Appendix. The condition number of the matrices in the equations depends on the relative contributions of the noise. The Labbé and Rousset algorithms took approximately 10 secs per frame to run.

Whilst the overall SSQ for the entire dataset was consistent with the noise model, the Krylov subspace approximation was not able to accurately distinguish between the different regional SSQs for a small number of interations. In principle, however, with a large enough amount of memory the algorithm would become increasingly more accurate. The Krylov subspace algorithms gave a good approximation to the SSQ for a single ROI. As the number of iterations was increased, so was the accuracy of the approximation (Figure 7). However, the increase in the number of iterations also required an increase in memory, and so would not allow the approximation to necessarily be used in practice on larger data sets.

4.1.2 Flumazenil Phantom via MRI segmentation

The recovered image from the simulation is shown in Figure 8. There was a good correlation between the recovered values and the simulated values (R= 0.98) in the grey and white regions (Table 2), although CSF regions were not well recovered. This is due to the low probability of the CSF in some regions, and the consequent difficulty in estimation. The actual values for the CSF, however, are not usually of interest, but it is important to include them in the model.

The algorithms speed is related directly to the number of regions and tissue classifications defined (rt). The time increases linearly (assuming the algorithm does not have to be split for memory purposes), with an addition of approximately 10-15 secs per extra classified region.

4.2 Measured Data Sets

4.2.1 Syringe Phantom

As can be seen (Table 3), the measured data sets were less well modelled by the noise characteristics, than the simulated data. This is not unexpected as the simulated data had perfect

Region	GM True	GM Rec	GM Sd	WM True	WM Rec	WM Sd
R Amygdala	7.21	5.32	0.35	0.48	1.25	0.33
L Amygdala	5.83	4.28	0.35	0.37	0.65	0.27
R Mid Inf Temp Gyrus	8.32	7.70	0.17	1.80	1.94	0.03
L Mid Inf Temp Gyrus	10.83	10.86	0.08	2.49	2.67	0.03
R Frontal Lobe	9.23	9.03	0.03	2.31	2.45	0.01
L Frontal Lobe	8.81	8.63	0.03	2.96	3.14	0.01
R Parietal Lobe	10.38	10.25	0.04	1.81	2.02	0.01
L Parietal Lobe	10.51	10.53	0.04	2.02	2.25	0.01
R Occipital Lobe	7.51	7.36	0.06	4.19	4.31	0.02
L Occipital Lobe	6.73	6.53	0.06	4.46	4.64	0.02
R Thalamus	4.76	5.09	0.18	1.81	1.88	0.03
L Thalamus	5.32	5.21	0.16	1.10	1.20	0.03
R Cerebellum	6.26	6.24	0.03	2.31	2.44	0.01
L Cerebellum	6.61	6.54	0.03	2.12	2.25	0.01

TABLE 2: Results from simulated [^{11}C]flumazenil data set: Grey Matter (GM) and White Matter (WM) V_D(ml/ml) values recovered by partial volume correction (Rec) for a representative set of anatomical regions and compared with the results pre correction.
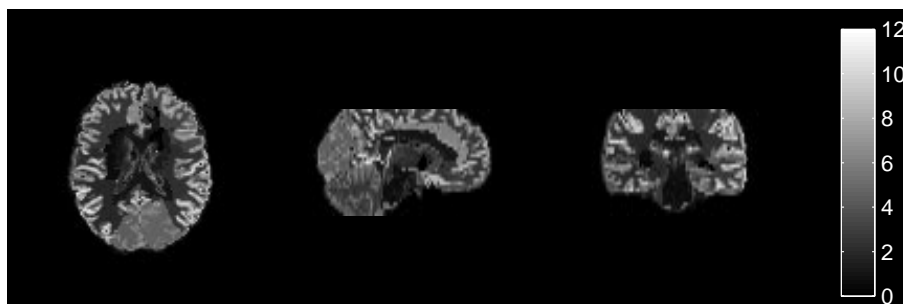

FIGURE 8: Simulated Flumazenil data projected onto MRI template.

noise specification. However, the new method gives apparently more plausible estimates for the error of the estimate, given the true value, especially in the higher noise frames.

As might have been expected, the Krylov algorithm did not allow for hypothesis testing of homogeneity. This was almost certainly due to inadequate specification of the noise model. The total SSQ was not as expected if the noise model had been correctly specified, and the SSQ of the single syringe was also affected this way. The noise model is of increasing importance from estimation of signal, errors through to hypothesis testing. In the case of hypothesis testing, the noise model must be assumed to be fully characterised, including a known variance. However with more accurate specification of the noise model, the possibility of hypothesis testing remains.

4.2.2 Measured Flumazenil

The flumazenil data was well recovered in the measured data (Figure 9, Table 4), except in the few regions where the grey/white border is less well defined (eg Occipital Lobe), giving the

| Method | Time | | 14.8mm | | | 11.9mm | | | 8.6mm | | | 4.7mm | | | Bgd | | |
	Start	Dur	NC	$\hat{x}$	$sd(\hat{x})$	NC	$\hat{x}$	$sd(\hat{x})$	NC	$\hat{x}$	$sd(\hat{x})$	NC	$\hat{x}$	$sd(\hat{x})$	NC	$\hat{x}$	$sd(\hat{x})$
Rousset	0	10	51.4	73.2	0.16	50.5	79.4	0.20	39.7	79.2	0.32	20.1	76.7	0.81	0.19	0.045	0.007
Labbe	0	10	51.4	74.0	0.28	50.5	80.0	0.37	39.7	80.3	0.63	20.1	83.7	1.73	0.19	0.040	0.011
Presented	0	10	51.4	72.7	0.80	50.5	78.2	1.01	39.7	78.5	1.52	20.1	75.1	3.59	0.19	0.049	0.036
Rousset	10	120	52.8	75.3	0.10	50.5	79.3	0.13	39.9	79.4	0.21	19.5	74.7	0.53	0.17	0.023	0.004
Labbe	10	120	52.8	75.7	0.09	50.5	79.8	0.12	39.9	81.0	0.21	19.5	77.6	0.59	0.17	0.019	0.004
Presented	10	120	52.8	74.8	0.24	50.5	78.7	0.30	39.9	78.3	0.46	19.5	73.4	1.08	0.17	0.025	0.011
Rousset	1200	10	52.8	75.3	0.20	52.5	82.4	0.26	40.9	81.6	0.41	19.9	76.1	1.03	0.20	0.048	0.008
Labbe	1200	10	52.8	75.3	0.38	52.5	82.9	0.51	40.9	81.7	0.87	19.9	80.2	2.41	0.20	0.047	0.015
Presented	1200	10	52.8	75.2	1.12	52.5	82.5	1.41	40.9	81.8	2.12	19.9	73.7	5.02	0.20	0.048	0.051
Rousset	1210	120	52.3	74.6	0.11	50.7	79.7	0.14	39.8	79.3	0.23	20.0	76.6	0.56	0.18	0.037	0.005
Labbe	1210	120	52.3	75.3	0.12	50.7	80.5	0.16	39.8	80.3	0.28	20.0	78.1	0.77	0.18	0.034	0.005
Presented	1210	120	52.3	74.0	0.33	50.7	79.1	0.42	39.8	78.4	0.63	20.0	76.7	1.50	0.18	0.040	0.015
Rousset	2400	10	53.8	76.7	0.26	52.6	82.6	0.34	37.5	74.8	0.55	16.8	64.0	1.37	0.22	0.072	0.011
Labbe	2400	10	53.8	76.5	0.54	52.6	82.8	0.72	37.5	75.4	1.22	16.8	73.0	3.38	0.22	0.070	0.021
Presented	2400	10	53.8	77.0	1.56	52.6	81.7	1.97	37.5	74.7	2.96	16.8	62.0	7.02	0.22	0.072	0.071
Rousset	2410	120	52.8	75.3	0.12	50.8	79.8	0.16	40.1	79.9	0.25	18.8	72.1	0.62	0.18	0.036	0.005
Labbe	2410	120	52.8	75.8	0.16	50.8	80.5	0.22	40.1	81.0	0.37	18.8	74.7	1.03	0.18	0.033	0.006
Presented	2410	120	52.8	74.9	0.45	50.8	79.1	0.57	40.1	79.5	0.86	18.8	71.9	2.05	0.18	0.038	0.021
Rousset	3600	10	56.5	80.5	0.35	50.1	78.7	0.46	35.5	70.8	0.73	16.8	64.1	1.84	0.21	0.064	0.015
Labbe	3600	10	56.5	80.8	0.75	50.1	80.4	1.00	35.5	74.2	1.70	16.8	72.4	4.71	0.21	0.057	0.029
Presented	3600	10	56.5	80.3	2.18	50.1	77.2	2.76	35.5	70.0	4.14	16.8	61.9	9.81	0.21	0.067	0.099
Rousset	3610	120	52.6	74.9	0.14	49.4	77.7	0.18	41.8	83.2	0.29	19.8	75.7	0.71	0.19	0.048	0.006
Labbe	3610	120	52.6	75.4	0.22	49.4	78.3	0.30	41.8	83.2	0.51	19.8	81.2	1.40	0.19	0.045	0.009
Presented	3610	120	52.6	74.5	0.64	49.4	77.2	0.80	41.8	83.8	1.21	19.8	74.1	2.86	0.19	0.050	0.029

TABLE 3: Results from partial volume correction of measured syringe data (Syringe diameters 14.8, 11.9, 8.6 and 4.7mm) from Rousset, Labbé and Presented method: value with no correction (NC) value after correction ($\hat{x}$) and estimated standard deviation of value ($sd(\hat{x})$). Initial activity value in all the syringes was 75 kBq/ml (at $t = 0$, all values are decay corrected to $t = 0$). Units are kBq/ml.

Region	GM Pre	GM Rec	GM Sd	WM Pre	WM Rec	WM Sd
R Amygdala	3.30	7.21	0.39	2.78	0.48	0.38
L Amygdala	4.01	5.83	0.40	2.68	0.37	0.31
R Mid Inf Temp Gyrus	5.51	8.32	0.20	3.56	1.80	0.04
L Mid Inf Temp Gyrus	5.90	10.83	0.09	3.91	2.49	0.04
R Frontal Lobe	5.78	9.23	0.03	3.55	2.31	0.01
L Frontal Lobe	5.35	8.81	0.03	3.91	2.96	0.01
R Parietal Lobe	5.85	10.38	0.05	2.98	1.81	0.01
L Parietal Lobe	5.74	10.51	0.05	3.07	2.02	0.02
R Occipital Lobe	5.47	7.51	0.07	4.86	4.19	0.03
L Occipital Lobe	5.42	6.73	0.06	4.77	4.46	0.03
R Thalamus	2.10	4.76	0.20	1.55	1.81	0.04
L Thalamus	3.06	5.32	0.19	1.13	1.10	0.03
R Cerebellum	4.29	6.26	0.03	2.88	2.31	0.01
L Cerebellum	4.49	6.61	0.03	3.03	2.12	0.01

TABLE 4: Results from measured [^{11}C]flumazenil data set: Grey Matter (GM) and White Matter (WM) V_D(ml/ml) values recovered by partial volume correction (Rec) for a representative set of anatomical regions and compared with results pre correction.

impression that the binding was taking place in the white matter. Again the CSF was highly variable and as such is not included in Table 4.

5   Discussion

The purpose of the present work was first; to bring together previous approaches to the PVC problem into a coherent mathematical framework, second; to devise rapid computational algorithms based on explicit definitions of noise models, and third; to explore the possibilities of obtaining further information on the associated errors, and questions about the homogeneity of the defined ROIs.

In the present paper partial volume effect models have been formulated in terms of linear matrix equations, in which the observed image is expressed as the product of the true concentration in a set of regions and matrices accounting for tissue fraction and point spread effects. The true local concentration is then estimated by the appropriate weighted least squares procedure. It is shown that the choice of algorithm for obtaining the least squares solution are dependent on the assumed noise models. Three noise models were considered; noise correlated by the PSF, uncorrelated noise, and a combination of both. Previous presentations of this problem in the literature have been principally concerned with algorithms for obtaining solutions but as a consequence have implicit assumptions about the noise model. The computational schemes presented here incorporate explicit assumptions. They differ with respect to ease of computation and inherent stability in the face of misspecification of the noise model.

Three aspects of the solution have been considered. First obtaining an estimate of the mean regional radioactivity. It is shown that this is relatively insensitive to the noise models in routine use. The principle assumption associated with this aspect of the solution is the homogeneity of
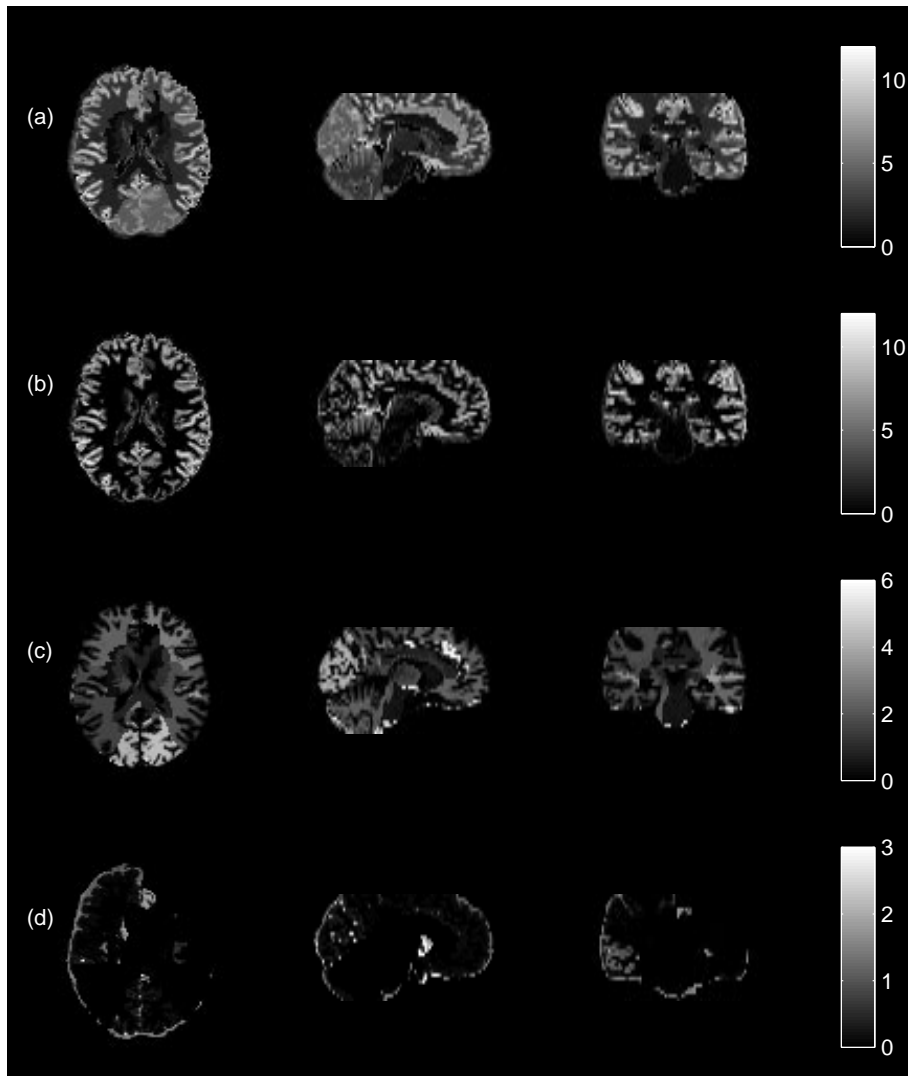
FIGURE 9: Measured Flumazenil data projected onto segmented MRI template after PVC;
(a) Total (b) Grey Matter (c) White Matter (d) CSF.

the ROIs and the correct classification of the tissue type within those ROIs. Rapid algorithms are presented here which enable partial volume corrected estimates to be readily calculated. The second aspect is obtaining an estimate of the variance of the estimates. As would be expected this is more dependent on the assumption of a correct noise model. The third aspect which was considered is the ability to test the assumed homogeneity of the ROIs. The Krylov method developed allows for hypothesis testing of inhomogeneity. However, in practice, this is limited by two factors. First as the volumes and number of tissues increase the memory required for the computations becomes too large on a standard desktop PC and second, that the approximation of the noise model for measured data is not sufficiently accurate.

In the simulations, realisations with noise of a completely characterised structure were presented, and it was shown that this resulted in good recovery of both the parameter estimates and the errors associated with them. However in practice it is well-known that the noise structure will not be perfectly characterised. It was seen in the true syringe phantom experiments that whilst this leads to estimates with greater variability than might be expected from the

simulations, the estimates themselves remain stable. The variability although increased is still a more accurate estimate of the variability than using error estimates derived from the models of either Rousset or Labbé. It was seen that the estimates are only as good as the underlying tissue data, and this was especially evident in the occipital cortex of the Flumazenil study. Here the grey matter / white matter boundary is less well defined than in other regions, and this leads to the estimates of the activity from the grey and white matter areas being difficult to distinguish. This is a problem in all techniques that use structural definition, especially when the structure cannot be well defined.

The nature of partial volume effects means that even if accurate an estimation technique is specified, and validated against phantom models, the underlying assumptions of tissue heterogeneity and the point spread effect are critical. In performing partial volume correction using MRI imaging, partial volume corrections are being based on information which is itself subject to partial volume effects albeit on a much smaller scale. True direct validation requires estimation and the recovery of tissue values from sources where these tissue values can also be directly measured outside the PET system. This is also true of validation of MRI segmentation techniques. Only a minority of partial volume techniques have considered this highly complex methodological problem (Iida et al., 2000), and this was not the focus of the work presented here. However, if models for the errors from this source were available, these could possibly be incorporated into the method presented.

The characterisation of the PSF is of central importance. The matrix formulation allows complex non-stationary characterisation. However, it is important to note that the algorithms presented here require that the PSF is separable, i.e. it can be applied independently in the x, y and z directions. The separability of the PSF was exploited in devising computationally fast algorithms. The dependence of the final estimates on the accuracy of the PSF characterisation has not been considered here, but would be dependent on ROI shape, noise in the image, tissue classification, shape of the PSF and relative FWHM, and would need testing for individual applications. Likewise we have not considered the effects of image misregistration, tissue misclassification (Meltzer et al., 1999; Reilhac et al., 2001), or ROI misplacement. Ideally these could be tested for in terms of inhomogeneity. The principal problems associated with this, however, is inadequate characterisation of the noise model as discussed above. Accurate characterisation of the noise model in image space is difficult but might be simplified by considering the problem in sinogram space (Carson, 1986). This would however offer challenges associated with specification of the model in sinogram space.

Computational schemes appropriate for the various noise models have been presented and are expanded further in the appendix. These schemes can be easily implemented and have proved to be very fast (e.g. the 43 region flumazenil volume with 3 tissue classifications is calculated in approximately 30 mins on a desktop computer). In principle, they can be applied to raw PET data, or to parametric images derived from application of temporal kinetic models to the raw data. Application to parametric images has the implicit assumption that the kinetic model is linear in the functional parameter. In this case, the non-correlated model, which requires no estimates of multiplicative noise, is probably sufficient to obtain an estimate of a classified regional activity together with its error.

Strictly, application to non-linear temporal kinetic modelling should be applied frame by frame. This has the advantages of allowing specification of a more accurate noise model including both

correlated and uncorrelated components, as well as producing error estimates which can then be utilised for weighting in the subsequent kinetic fitting. Estimates of the additive noise component can be obtained from the background. In practice, however effects of the non-linearity can be assessed in individual cases and the simpler uncorrelated PVC model applied to the parametric image, if the bias is considered acceptable.

A   Algorithms for 3-D Implementation

A.1   Tensor Implementation

There is an inherent 3-dimensional structure in the data. Methods such as Labbé (1996) , while designing complex matrix algorithms to account for this structure, fail to make use of it in the algorithm for solution. Methods such as Rousset (Rousset et al., 1998), did use this structure but through the time consuming process of an analytical simulator. Further, the use of an analytical simulator does not lend itself easily to the calculation of errors.

The algorithm proposed here will allow easy specification of a spatially variant PSF, with the assumption of separability in the 3 cartesian axes. This is the equivalent assumption to Labbé, but with the added advantage of allowing for a spatially variant PSF.
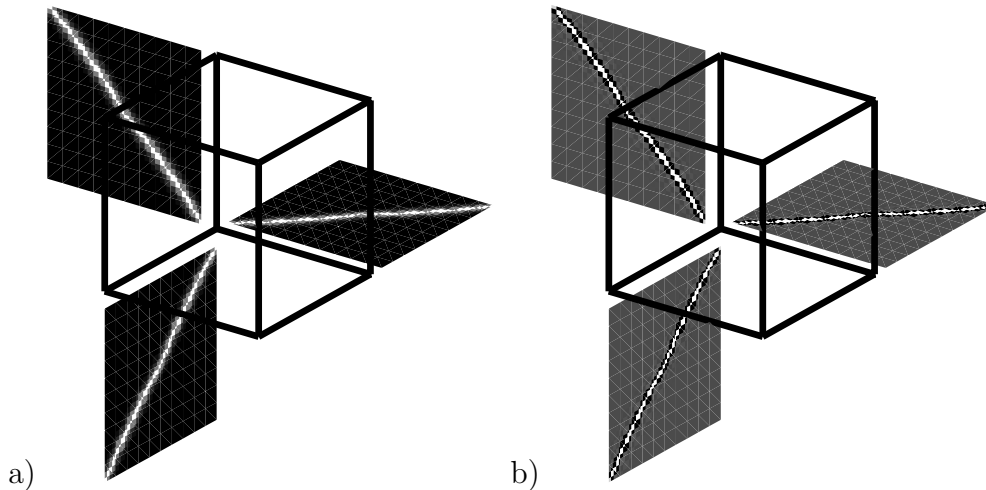

FIGURE 10: : a) Tensor point spread operator, b) Tensor recover operator.

A tensor can be thought of as a multi-dimensional matrix. The PSF specification is then classed as a 6-D tensor taking ((x,y,z),(x',y'z')) co-ordinate structures so that any point is related to the space that the point is blurred to. The condition of separability allows the 6-D tensor to be written as a product of three 2-D tensors relating (x,x'), (y,y') and (z,z') (see Figure 10). Thus the tensor product becomes a series of matrix multiplications, which are fast and simple to compute. This process is also applicable to the weighting matrix for the purely uncorrelated and purely correlated cases. For the more complex correlated noise model other methods are required and developed below (see A.2).

The algorithm applies the PSF to the native 3-D volume without requiring vectorisation of the image. All operations are thought of as multi-dimensional operations as opposed to the uni (vector) or bi (matrix) dimensional operations of other methods. Thus the solution may be written in tensor notation as,

$$x_{r_1} = (R_{r_1 z_1 y_1 x_1} W_{x_1 y_1 z_1 z_2 y_2 x_2} R_{x_2 y_2 z_2 r_2})^{-1}...$$
$$R_{r_2 z_3 y_3 x_3} W_{x_3 y_3 z_3 z_2 y_4 x_4} P_{x_4 y_4 z_4 z_5 y_5 x_5} b_{x_5 y_5 z_5}, \tag{19}$$

using the summation notation convention. The inverse, in Eqn 19, is simply a 2D matrix inverse.

For the different noise models these equations lead to slightly different algorithms. In the purely uncorrelated and purely correlated (no uncorrelated component) cases this equation can be used to estimate both the signal ($\hat{x}$) and errors ($var(\hat{x})$) since P and W are separable. However, the correlated noise case requires an extra algorithm because although P is well specified in a separable tensor notation, W is not (even though W^{-1} can be specified in a separable tensor notation). This algorithm could be described in terms of a constrained noise algorithm, where the uncorrelated component of the noise acts as a regularisation parameter. A very small component of uncorrelated noise causes large variance in the estimates of an algorithm that does not take this possibility into account. This is due to the condition number of the matrices involved. However the addition of the uncorrelated component term accounts for this problem and as such acts as a regularisation term for the algorithm.

A.2 Estimation of $\hat{x}$ and var($\hat{x}$) with Correlated Noise

For the correlated noise model an iterative method can be used to circumvent the non-separability of the weighting matrix. The inverse of the weighting matrix is separable and this lends itself to the iterative solution of $Z = WR$. Estimates of Z are updated via a suitable scheme until $W^{-1}Z = R$.

A.2.1 Iterative Method

A first-order stationary iterative scheme was chosen which converges in all cases and has a suitably bounded convergence parameter (see below). The algorithm for the correlated noise model is,

$$Z_{n+1} = (1 - \tau)Z_n + \tau \frac{1}{\sigma_u^2} P^T P(R - \Lambda(Rx)Z_n) \tag{20}$$

where τ is a relaxation parameter which is calculated at the beginning of the algorithm to ensure convergence.

The solution Z is then incorporated into the weighted least squares solution as,

$$\hat{x} = (Z^T R)^{-1} Z P^{-1} b, \tag{21}$$

and for the variance estimate as,

$$var(\hat{x}) = \frac{(Z^T R)^{-1} Z^*(Rx - P^{-1}b)}{N_{Vox} - N_{ROI}}, \tag{22}$$

where $Z^* = (Rx - P^{-1}b)^T W$ is solved using the same iterative procedure.

A.2.2 Proof of Convergence

Let $C = \sigma_u^2 P^{-1}(P^{-1})^T$ and $W = (D + \sigma_u^2 (P^{-1})^T P^{-1})^{-1}$ as above. Then the iterative scheme (Eqn 20) is given by,

$$Z_{n+1} = Z_n + \tau C^{-1}(R - W^{-1}Z_n) \tag{23}$$

If C^{-1} and W^{-1} are positive definite (which is elementary from their definitions) then the iterative scheme will converge for $0 \leq \tau \leq \frac{2}{\lambda_n}$ where λ_n is the maximal eigenvalue of $C^{-1}W^{-1}$ (Axelsson, 1994, Theorem 5.6).

Thus, to guarantee convergence, it remains to calculate an upper bound for the maximal eigenvalue of $C^{-1}W^{-1}$ which enables an appropriate selection of τ.

$$
\begin{aligned}
C^{-1}W^{-1} &= \frac{1}{\sigma_u^2} P^T P (D + \sigma_u^2 (P^{-1}P^{-1})^T) \\
&= \frac{1}{\sigma_u^2} P^T P D + I
\end{aligned}
\tag{24}
$$

where I is the identity matrix. The eigenvalues of $C^{-1}W^{-1}$ are the eigenvalues of a product of a positive definite matrix $P^T P$ and a diagonal matrix plus the identity matrix. A corollary (Axelsson, 1994, Corollary 3.14) of the Courant-Fischer theorem (Axelsson, 1994, Lemma 3.13) gives an upper bound for the maximal eigenvalue in the case of a product of a positive definite matrix ($P^T P$) and a matrix with non-negative maximal eigenvalue (D). The addition of the identity matrix simply adds 1, giving,

$$\lambda_{max}(C^{-1}W^{-1}) \leq \frac{1}{\sigma_u^2} \ s_{max}(P)^2 \ \lambda_{max}(D) + 1 \tag{25}$$

where s_{max} is the maximum singular value and λ_{max} is the maximum eigenvalue. $\lambda_{max}(D)$ is the largest element of D and $s_{max}(P)$ is the product of the maximal singular values of each cartesian component of P.

A value for τ that guarantees convergence of the iterative scheme can then be chosen as

$$\tau = \frac{2\sigma_u^2}{s_{max}(P)^2 \ \lambda_{max}(D) + 1} \tag{26}$$

A.3   Inhomogeneity Testing

The above algorithms allow estimates of the signal and its associated error. However, they do not facilitate the estimation of the regional SSQ, which is required for inhomogeneity testing. However, there are approximational methods that will in principle converge to the correct value of the regional SSQ allowing the possibility of inhomogeneity testing. However this is highly dependent on the correct specification of the noise model.

If the ROI is defined in a deterministic sense in contrast to a probabilistic sense, then in principle inhomogeneity testing is possible. The ROIs represented in the R matrix can each be associated with a sum of squares error, independently of the other ROIs due to their orthogonal nature (by definition if they are not probabilistically defined). However, implementation requires knowledge of the correctly weighted residuals for each of the orthogonal ROIs which depends on the weighting matrix.

Krylov subspace methods are adept at estimating the square root of symmetric matrices (where the square root is defined to also be symmetric allowing it to be uniquely defined). These methods have previously been rigorously analyzed for deconvolution (Schneider and Willsky, 2001), but not for inhomogeneity testing.

The major advantages of using a Krylov algorithm is that the matrix that a square root is required for is not altered by the algorithm (Golub and Van Loan, 1983) so only a method of applying the matrix to vectors is needed and hence we can make use of the Tensor structures already defined to allow the computation A.1.

In order to evaluate the square root matrix equation, we make use of the Lanczos Algorithm (Golub and Van Loan, 1983) and its extensions to matrix square roots (Allen et al., 2000). The results from the algorithm allow estimation of the regional sum of squares

$$SSQ_{ROI} = (Rx - P^{-1}b)^T W^{\frac{1}{2}} R_{ROI}^T R_{ROI} W^{\frac{1}{2}} (Rx - P^{-1}b) \tag{27}$$

It is known that if the noise model is correctly specified including the underlying value of σ_g^2 then the total sum of squares error will be distributed χ^2 with degrees of freedom equal to the number of data points. This is also true on a subset of the regions if they are independent from the other regions. Thus if we want to test the homogeneity of a region, we just test the regional sum of squares error against the size of the region, assuming the correctly specified noise model.

$$SSQ_{ROI} \sim \chi^2(\|ROI\|_0) \tag{28}$$

B Glossary

B.1 Variables and Functions

Symbol	Description
P	Point spread operator
R	Region of interest definition
T	Tissue classification
b	Measured image
x	True PVC corrected tracer activities
W	Weighting matrix
I	Identity matrix
n	Number of Voxels
r	Number of Regions in R
t	Number of Classifications in T
$\odot$	Khatri-Rao row product (see B.2)
$\Lambda()$	Diagonal matrix
$\lambda_{max}()$	Maximum eigenvalue
$s_{max}()$	Maximum singular value
τ	Relaxation parameter
η_p	Poisson noise process
η_g	Gaussian noise process
σ_g	Gaussian noise std
SSQ_{ROI}	Residual sum of squares for an ROI

B.2 Khatri-Rao Row Product ($\odot$)

This product is the row-wise kronecker ($\otimes$)product between the rows of A, a $k \times m$ matrix and B, a $k \times n$ matrix giving a $k \times mn$ matrix (Rao and Mitra, 1971). The product takes the following form

$$A \odot B = \begin{bmatrix} a_1 \otimes b_1 \\ a_2 \otimes b_2 \\ \cdots \\ a_k \otimes b_k \end{bmatrix} = \begin{bmatrix} a_{11}b_1 \ a_{12}b_1 \ \cdots \ a_{1n}b_1 \\ a_{21}b_2 \ a_{22}b_2 \ \cdots \ a_{2n}b_2 \\ \cdots \\ a_{k1}b_k \ a_{k2}b_k \ \cdots \ a_{kn}b_k \end{bmatrix} \tag{29}$$

where a_{ij} is the $i - j$ element of A and a_i, b_i are the ith rows of A and B respectively.

Acknowledgements

The authors would like to thank Peter Neelin and Federico Turkheimer for useful discussions, as well as two anonymous referees for their constructive comments.

References

Allen, E. J., Baglama, J., and Boyd, S. K. (2000). Numerical approximation of the product of the square root of a matrix with a vector. *Linear Algebra and Its Applications*, 310(1-3):167–181.

Ashburner, J. and Friston, K. (1997). Multimodal image coregistration and partitioning–a unified framework. *Neuroimage*, 6(3):209–17.

Ashburner, J. and Friston, K. J. (1999). Nonlinear spatial normalization using basis functions. *Hum Brain Mapp*, 7(4):254–66.

Asselin, M.-C., Cunningham, V. J., Turjanski, N., Wahl, L. M., Bloomfield, P. M., Gunn, R. N., and Nahmias, C. (2001). Venous sinuses vs on-line arterial sampling as input functions in PET. In A. Gjedde, S. B. Hansen, G. M. K. and Paulson, O. B., editors, *Physiological Imaging of the Brain with PET*, pages 73–81. Academic Press.

Aston, J. A. D., Gunn, R. N., Worsley, K. J., Ma, Y., Evans, A. C., and Dagher, A. (2000). A statistical method for the analysis of positron emission tomography neuroreceptor ligand data. *Neuroimage*, 12:245–256.

Axelsson, O. (1994). *Iterative solution methods*. Cambridge University Press, Cambridge New York.

Bailey, D. L. (1992). 3d acquisition and reconstruction in positron emission tomography. *Ann Nucl Med*, 6(3):123–30.

Bailey, D. L. and Meikle, S. R. (1994). A convolution-subtraction scatter correction method for 3d pet. *Physics in Medicine and Biology*, 39(3):411–424.

Bailey, D. L., Young, H., Bloomfield, P. M., Meikle, S. R., Glass, D., Myers, M. J., Spinks, T. J., Watson, C. C., Luk, P., Peters, A. M., and Jones, T. (1997). ECAT ART - a continuously rotating PET camera: Performance characteristics, initial clinical studies, and installation considerations in a nuclear medicine department. *European Journal of Nuclear Medicine*, 24(1):6–15.

Carson, R. E. (1986). A maximum likelihood method for region-of-interest evaluation in emission tomography. *J Comput Assist Tomogr*, 10(4):654–63.

Carson, R. E., Yan, Y., Daubewitherspoon, M. E., Freedman, N., Bacharach, S. L., and Herscovitch, P. (1993). An approximation formula for the variance of PET region-of-interest values. *Ieee Transactions on Medical Imaging*, 12(2):240–250.

Golub, G. H. and Van Loan, C. F. (1983). *Matrix Computations*. The Johns Hopkins University Press, Baltimore, USA.

Grootoonk, S. (1995). *Dual energy window correction for scattered photons in 3D positron emission tomography*. PhD thesis, University of Surrey.

Hammers, A., Koepp, M. J., Free, S., Brett, M., Richardson, M. P., Labbé, C., Cunningham, V. J., Brooks, D. J., and Duncan, J. S. Implementation and application of a new brain template for multiple volumes of interest. *Human Brain Mapping*, in press.

Hoffman, E. J., Huang, S. C., and Phelps, M. E. (1979). Quantitation in positron emission computed tomography: 1. effect of object size. *J Comput Assist Tomogr*, 3(3):299–308.

Holmes, C. J., Hoge, R., Collins, L., Woods, R., Toga, A. W., and Evans, A. C. (1998). Enhancement of mr images using registration for signal averaging. *J Comput Assist Tomogr*, 22(2):324–33.

Iida, H., Law, I., Pakkenberg, B., Krarup-Hansen, A., Eberl, S., Holm, S., Hansen, A. K., Gundersen, H. J., Thomsen, C., Svarer, C., Ring, P., Friberg, L., and Paulson, O. B. (2000). Quantitation of regional cerebral blood flow corrected for partial volume effect using O-15 water and PET: I. theory, error analysis, and stereologic comparison. *J Cereb Blood Flow Metab*, 20(8):1237–51.

Karp, J. S., Daube-Witherspoon, M. E., and Muehllehner, G. (1991). Factors affecting accuracy and precision in PET volume imaging. *J Cereb Blood Flow Metab*, 11(2):A38–44.

Kinahan, P. E. and Rogers, J. G. (1989). Analytic 3D image-reconstruction using all detected events. *Ieee Transactions on Nuclear Science*, 36(1):964–968.

Koepp, M. J., Richardson, M. P., Brooks, D. J., Poline, J. B., Van Paesschen, W., Friston, K. J., and Duncan, J. S. (1996). Cerebral benzodiazepine receptors in hippocampal sclerosis. an objective in vivo analysis. *Brain*, 119 (Pt 5):1677–87.

Labbé, C., Froment, J. C., Kennedy, A., Ashburner, J., and Cinotti, L. (1996). Positron emission tomography metabolic data corrected for cortical atrophy using magnetic resonance imaging. *Alzheimer Dis Assoc Disord*, 10(3):141–70.

Labbé, C., Koepp, M. J., Ashburner, J., Spinks, T., Richardson, M., Duncan, J., and Cunningham, V. J. (1998). Absolute PET quantification with correction for partial volume effects within cerebral structures. In R. E. Carson, M. E. D.-W. and Herscovitch, P., editors, *Quantative Functional Brain Imaging with Positron Emission Tomography*, pages 59–66.

Law, I., Iida, H., Holm, S., Nour, S., Rostrup, E., Svarer, C., and Paulson, O. B. (2000). Quantitation of regional cerebral blood flow corrected for partial volume effect using O-15 water and PET: Ii. normal values and gray matter blood flow response to visual activation. *J Cereb Blood Flow Metab*, 20(8):1252–63.

Leahy, R. M. and Qi, J. Y. (2000). Statistical approaches in quantitative positron emission tomography. *Statistics and Computing*, 10(2):147–165.

Lemieux, L., Hagemann, G., Krakow, K., and Woermann, F. G. (1999). Fast, accurate, and reproducible automatic segmentation of the brain in T1-weighted volume MRI data. *Magn Reson Med*, 42(1):127–35.

Mazziotta, J. C., Phelps, M. E., Plummer, D., and Kuhl, D. E. (1981). Quantitation in positron emission computed tomography: 5. physical– anatomical effects. *J Comput Assist Tomogr*, 5(5):734–43.

McCullagh, P. and Nelder, J. A. (1989). *Generalized linear models*. Chapman and Hall, London New York, 2nd – edition.

Meltzer, C. C., Cantwell, M. N., Greer, P. J., Ben-Eliezer, D., Smith, G., Frank, G., Kaye, W. H., Houck, P. R., and Price, J. C. (2000). Does cerebral blood flow decline in healthy aging? a PET study with partial-volume correction. *J Nucl Med*, 41(11):1842–8.

Meltzer, C. C., Kinahan, P. E., Greer, P. J., Nichols, T. E., Comtat, C., Cantwell, M. N., Lin, M. P., and Price, J. C. (1999). Comparative evaluation of MR-based partial-volume correction schemes for PET. *J Nucl Med*, 40(12):2053–65.

Meltzer, C. C., Leal, J. P., Mayberg, H. S., Wagner, H. N., J., and Frost, J. J. (1990). Correction of PET data for partial volume effects in human cerebral cortex by MR imaging. *J Comput Assist Tomogr*, 14(4):561–70.

Muller-Gartner, H. W., Links, J. M., Prince, J. L., Bryan, R. N., McVeigh, E., Leal, J. P., Davatzikos, C., and Frost, J. J. (1992). Measurement of radiotracer concentration in brain gray matter using positron emission tomography: Mri-based correction for partial volume effects. *J Cereb Blood Flow Metab*, 12(4):571–83.

Pajevic, S., Daube-Witherspoon, M. E., Bacharach, S. L., and Carson, R. E. (1998). Noise characteristics of 3-D and 2-D PET images. *IEEE Trans Med Imaging*, 17(1):9–23.

Rao, C. R. and Mitra, S. K. (1971). *Generalized inverse of matrices and its applications.* Wiley, New York.

Reilhac, A., Theil, A., Frouin, V., Collins, L., Rousset, O., and Evans, A. C. (2001). Automated partial volume correction: Simulation-based assessment of errors. *Journal of Cerebral Blood Flow and Metabolism*, 21(S1):S546.

Richardson, M. P., Koepp, M. J., Brooks, D. J., Fish, D. R., and Duncan, J. S. (1996). Benzodiazepine receptors in focal epilepsy with cortical dysgenesis: an 11c-flumazenil pet study. *Ann Neurol*, 40(2):188–98.

Rousset, O., Ma, Y., Kamber, M., and Evans, A. C. (1993). 3D simulations of radiotracer uptake in deep nuclei of human brain. *Comput Med Imaging Graph*, 17(4-5):373–9.

Rousset, O. G., Deep, P., Kuwabara, H., Evans, A. C., Gjedde, A. H., and Cumming, P. (2000). Effect of partial volume correction on estimates of the influx and cerebral metabolism of 6-[(18)f]fluoro-l-dopa studied with PET in normal control and parkinson's disease subjects. *Synapse*, 37(2):81–9.

Rousset, O. G., Ma, Y., and Evans, A. C. (1998). Correction for partial volume effects in PET: principle and validation. *J Nucl Med*, 39(5):904–11.

Schneider, M. K. and Willsky, A. S. (2001). Krylov subspace estimation. *Siam Journal on Scientific Computing*, 22(5):1840–1864.

Slifstein, M., Mawlawi, O., and Laruelle, M. (2001). Partial volume effect correction: Methodological considerations. In A. Gjedde, S. B. Hansen, G. M. K. and Paulson, O. B., editors, *Physiological Imaging of the Brain with PET*, pages 65–71. Academic Press.

Watson, C. C., Newport, D., and Casey, M. (1996). A single-scatter simulation technique for scatter correction in 3D PET. In Amans, P. G. and JL, editors, *Three-Dimensional Image Reconstruction in Radiation and Nuclear Medicine.*, pages 255–268. Kluwer Academic Publishers, Dordrecht.